Continuous change detection outperforms traditional post-classification change detection for long-term monitoring of wetlands

Quentin Demarquet, Sébastien Rapinel, Olivier Gore, Simon Dufour, Laurence Hubert-Moy

International Journal of Applied Earth Observation and Geoinformation 133 (2024) 104142

Contents lists available at ScienceDirect

International Journal of Applied Earth Observation and Geoinformation

journal homepage: www.elsevier.com/locate/jag

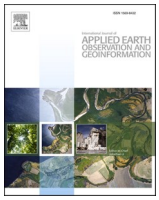

Continuous change detection outperforms traditional post-classification change detection for long-term monitoring of wetlands

Quentin Demarquet [a], Sébastien Rapinel [a], Olivier Gore [b], Simon Dufour [a], Laurence Hubert-Moy [a,*]

[a] Université Rennes 2, LETG UMR 6554 CNRS, place du recteur Henri Le Moal, 35000 Rennes, France
[b] Établissement Public du Marais Poitevin, 1 Rue Richelieu, 85400 Luçon, France

ARTICLE INFO

Keywords:
CCDC
Time-series analysis
Google Earth Engine
Landsat
Habitat monitoring

ABSTRACT

Accurate long-term monitoring of wetlands using satellite archives is crucial for effective conservation. While new methods based on temporal profile classification have been useful for long-term monitoring of wetlands, their advantages over traditional classification methods have not yet been demonstrated. This study aimed to compare continuous change detection (using the continuous change detection and classification (CCDC) algorithm) to traditional post-classification change detection for monitoring wetland changes between 1984 and 2022 in a temperate coastal marsh (Marais Poitevin, France) from the Landsat archive. The reference dataset was collected mainly from field observations and used to train and test a random forest classifier. The accuracy of the resulting change map was then assessed for both methods using validation points collected *via* visual interpretation of historical aerial photographs and Landsat temporal profiles. The change map derived from CCDC had much higher unbiased overall accuracy (0.86 ± 0.02) than that derived from post-classification change detection (0.51 ± 0.03). In addition, wetland loss was much higher than wetland gain (18 % and 2 % of the area, respectively) and was due mainly to conversion of grassland to cropland and urbanization. The study demonstrated that, unlike traditional post-classification change detection, continuous change detection provides maps of wetland changes sufficiently accurate for operational use by managers. The study also confirmed the ongoing impact of agricultural intensification and artificialization on wetland degradation in Europe.

1. Introduction

Wetlands, defined as "areas that are inundated or saturated at a frequency to support, and which normally do support, plants adapted to saturated and/or inundated conditions" (Brinson, 1993), provide 40 % of the total value of ecosystem services on Earth (Xu et al., 2020). However, the amount of ecosystem services provided has decreased continuously for several decades due to human pressure on wetlands, as well as climate change (Yang et al., 2023). From a conceptual viewpoint, it is useful to distinguish existing wetlands that are slightly or not impacted by human or climate disturbances from damaged wetlands degraded by changes in land use and land cover (LULC) and from habitat types, such as crops or permanent ponds, in which restoration can be performed (Rapinel et al., 2018). Long-term (i.e. several decades) mapping of LULC or habitat types is therefore a key indicator for monitoring the structure of wetlands and ultimately their ability to provide ecosystem services and support human well-being (Yang et al., 2023).

Earth observation (EO) data, which provide standardized, repeated measurements with wide spatial coverage, have been extensively used to detect long-term changes in wetlands (Jafarzadeh et al., 2022). Among EO data, archive images from Landsat missions are of particular interest for long-term monitoring, since Landsat images have been collected every 16 days at 30 m spatial resolution since 1984, making them the longest EO record worldwide (Wulder et al., 2022). In addition, the Landsat archive is freely available and integrated into cloud-computing platforms such as Google Earth Engine (Gorelick et al., 2017).

Currently, using the Landsat archive to detect changes in wetlands is based mainly on two methods: traditional post-classification change detection or continuous change detection (Demarquet et al., 2023). The former involves classifying LULC or habitat types for two separate years from one or a few cloud-free images or one composite image, then detecting changes between the two years by combining the classifications in post-processing (Zhu, 2017). The value of this simple method is

* Corresponding author.
E-mail address: laurence.hubert@univ-rennes2.fr (L. Hubert-Moy).

https://doi.org/10.1016/j.jag.2024.104142
Received 10 April 2024; Received in revised form 27 August 2024; Accepted 1 September 2024
Available online 6 September 2024

that it requires few images and therefore few computational resources (Zhu, 2017). The latter method, which is more recent, identifies and classifies temporal segments (each corresponding to one LULC/habitat type) identified from a dense Landsat time-series containing several hundred observations. This method has been developed using a variety of algorithms, such as LandTrendr (Kennedy et al., 2010) or continuous change detection and classification (CCDC) (Zhu and Woodcock, 2014a). The advantage of continuous change detection is that it can produce a LULC/habitat map for any year in the period under consideration from a single classifier. Initially, continuous change detection was rarely used due to the high computation time and number of images needed; however, it is increasingly used due to the recent development of cloud-computing application programming interfaces (APIs) (Pasquarella et al., 2022).

Although continuous change detection would appear more effective than post-classification change detection, the latter remains the most widely used method for monitoring long-term changes in wetlands (Demarquet et al., 2023; Jafarzadeh et al., 2022). Moreover, recent studies that used the Landsat archive for long-term wetland monitoring emphasized that the overall accuracy of LULC or habitat maps was high (>0.80) regardless of the method. For example, LULC maps of a coastal wetland had an overall accuracy of 0.90–0.97 using post-classification change detection (Hotaiba et al., 2024) and 0.88 using continuous change detection (Peng et al., 2021). Similarly, LULC maps of an inland marsh had an overall accuracy of 0.82–0.88 using post-classification change detection (Liu et al., 2021) and 0.84 using continuous change detection (Fu et al., 2022). These results indicate two main reasons why choosing the most appropriate method to detect wetland change can be difficult: (i) the classification accuracy obtained for one site using a given method cannot be strictly compared to that obtained for another site using another method, since accuracy depends on the structural and functional characteristics of the site, and (ii) the accuracy of change maps is rarely specified for post-classification change detection (Demarquet et al., 2023).

The objective of the present study was to determine which method detected long-term wetland changes most accurately. To this end, the two methods used the Landsat archive to detect changes in a coastal marsh in France between 1984 and 2022. Specifically, continuous change detection was performed using the most widely used CCDC algorithm (Pasquarella et al., 2022). We then assessed the overall accuracy of the change map generated by each method and also assessed strengths and weaknesses of each method.

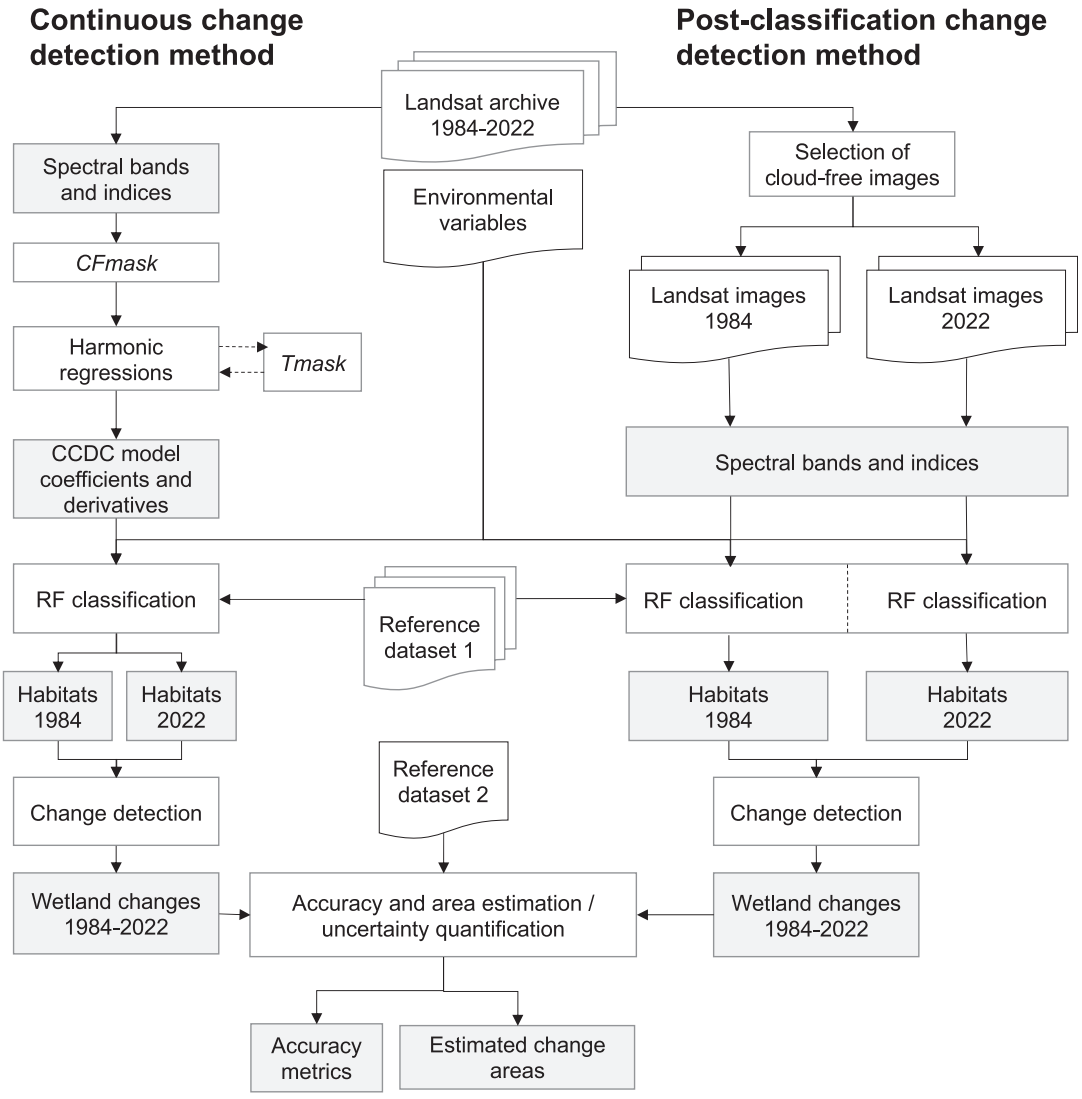

Fig. 1. Framework for monitoring long-term changes using the Landsat archive and the continuous change detection and classification (CCDC) algorithm and comparison with the post-classification change detection method. RF: random forest.

2. Materials and methods

2.1. Rationale of the approach

Continuous and post-classification change detection methods were performed in parallel (Fig. 1) using the same Landsat archive, environmental variables, and reference datasets. The first reference dataset (Dataset 1), which included field archive data supplemented with points extracted from visual interpretation of historical aerial photographs, was used to evaluate the accuracy of annual habitat maps. The second reference dataset (Dataset 2), which included points extracted from visual interpretation of aerial photographs, satellite images from Google Earth, and temporal profiles derived from the Landsat archive, was used to evaluate the accuracy of the change detection maps. Continuous change detection was performed using the API developed by Arévalo et al. (2020) in the Google Earth Engine (GEE) cloud-computing platform (Gorelick et al., 2017).

Habitats were characterized using the hierarchical European Nature Information System (EUNIS) level 1 classification (Davies et al., 2004). EUNIS classes were grouped into two classes (i.e., damaged wetlands or existing wetlands, which were strongly altered by or protected from human disturbance, respectively) to describe wetland changes (Rapinel et al., 2018).

2.2. Study site

The Marais Poitevin, located on the Atlantic coast of France (Fig. 2), is the second largest wetland in the country (ca. 100 000 ha). This coastal wetland complex has a temperate climate and flat topography whose elevation ranges from 0 to 10 m. Construction of dikes and canals for agriculture and urbanization since the 13th century has resulted in marsh drainage (Godet and Thomas, 2013; Pouzet et al., 2015). Today, the Marais Poitevin includes three contrasting areas: a western area with marine and coastal habitats, a central area with wet grasslands and cropland, and an eastern area with wet grasslands and woodlands (Rapinel et al., 2015). Pressure from tourism and farming has prompted the creation of several protected areas over the past few decades (i.e., Natura 2000 sites, nature reserves, and regional nature parks). Nonetheless, the wetlands have generally degraded over time despite these conservation measures (Duncan et al., 1999).

2.3. Data

2.3.1. Landsat images

Landsat TM, ETM+, OLI/TIRS, and OLI2/TIRS2 atmospherically corrected surface images (Tier 1, Collection 2, Level 2) acquired from 1984 to 2022 were used and accessed through GEE (USGS, 2021). The images were selected because enhanced geometric correction and radiometric calibration and harmonization among sensors makes the images suitable for time-series analysis (Dwyer et al., 2018). The study site was covered by two tiles – path/row 200/28 and 201/28 (Fig. 2) – for which 800 and 784 images were retrieved, respectively. Optical and thermal band time series were used as input data. Optical bands were used to generate the eight spectral indices that were set by default in the Google Earth Engine CCDC application programming interface (Arévalo et al., 2020) (Table 1). Clouds, shadows, and noise were removed from Landsat images using the *CFMask* algorithm (Foga et al., 2017), which is a C version of the popular *FMask* algorithm v3.3 (Zhu and Woodcock,

Table 1
Summary of spectral bands and indices derived from the Landsat archive used in the study.

Input data	Description	Source
Spectral bands	Landsat spectral bands (visible, NIR, and SWIR) in surface reflectance, and thermal bands in surface temperature	–
NDVI	Normalized Difference Vegetation Index: used to quantify vegetation health and density related to photosynthesis	Myneni et al. (1995)
EVI	Enhanced Vegetation Index: used to quantify vegetation health and density with higher sensitivity in high-biomass regions; related to canopy structure	Huete et al. (2002)
EVI2	Two-band Enhanced Vegetation Index: EVI calculated without the blue spectral band to calculate EVI based on sensors lacking a blue band (e.g., AVHRR)	Jiang et al. (2008)
NBR	Normalized Burn Ratio: used to identify burned areas and quantify fire severity	Key and Benson (2006)
NDFI	Normalized Difference Fraction Index: used to monitor forest degradation and deforestation; sensitive to canopy state. Calculated from green vegetation (GV), non-photosynthetic vegetation (NPV), soil, and shade fractions obtained from spectral mixture analysis.	Souza et al. (2005)
Greenness vegetation index	Greenness fraction: extracted by tasseled cap transformation; corresponds to vegetation fraction	Crist (1985)
Brightness vegetation index	Brightness fraction: extracted by tasseled cap transformation; corresponds to soil fraction	Crist (1985)
Wetness vegetation index	Wetness fraction: extracted by tasseled cap transformation; corresponds to the relation between soil and canopy wetness	Crist (1985)

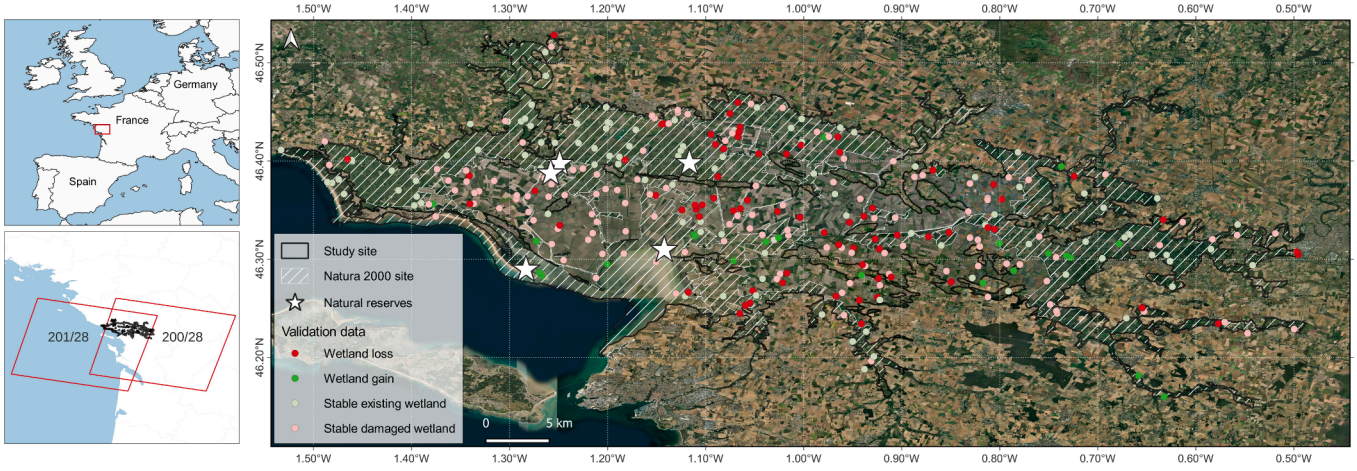

Fig. 2. Location of the study area and Landsat tile overlay (left) and reference Dataset 2 used to assess the unbiased accuracy of the change map (right).

2014a).

2.3.2. Environmental variables

Environmental variables were added to the Landsat data to better distinguish wetland habitats (Demarquet et al., 2023). They included three topographic variables (i.e., elevation, slope, and aspect) derived from the DEM SRTM at 30 m resolution (Farr et al., 2007), as well as the distance to the sea calculated at 30 m spatial resolution from the highest sea level (IGN, Shom, 2009).

2.3.3. Historical aerial photographs

A total of 16 aerial photographs covering different parts of the study site from 1984–1997 were downloaded from the French National Geographic Institute (IGN) website available in open access (https://remonterletemps.ign.fr/): 6 black-and-white photographs from 1984 (1:30 000 scale) and 10 RGB color photographs from 1990 and 1997 (ranging from 1:21 000 to 1:26 000 scale). The photographs were georeferenced using ground control points obtained from 2022 aerial photographs orthorectified using QGIS software (QGIS Development Team, 2018), achieving an average root mean square error of 3.58 m.

2.3.4. Field data

Field vegetation and LULC data were collected from several international, national, and local archive databases (Table 2). Field vegetation data included vegetation maps and phytosociological relevés. Local botanists have produced vegetation maps since the early 2000s to monitor protected areas. Vegetation maps of natural reserves (EUNIS 2004 and PVF) and the Natura 2000 habitat map described vegetation at the habitat or phytosociological unit scale. The former map covered 18 km^2 on five nature reserves (Fig. 2), while the latter covered the entire site. The vegetation relevés (EUNIS 2020) consisted of 821 phytosociological relevés collected mainly on grasslands by local botanists and scientists. The relevés were automatically assigned to EUNIS habitats using the EUNIS-ESy expert system (Chytrý et al., 2020).

Field LULC data were obtained from the land parcel information system (LPIS), the land use and cover area frame survey (LUCAS), and two local GIS layers related to agri-environmental measures (i.e., "arable land conversion" and "communal grasslands"). The LPIS contains farmers' annual declarations of crop type in each field, in the framework of the European Union's Common Agricultural Policy (CAP) (European Court of Auditors, 2016). This geographic information layer, released every year since 2007, describes ca. 30 crop classes, including grassland. Each year, it lists several hundred fields in the Marais Poitevin. The LUCAS database provided field observations of LULC types from a regular sampling campaign across Europe in 2006, 2012, and 2018 (Palmieri, 2016), which included 103, 70, and 69 points in the Marais Poitevin, respectively. The two local GIS layers described 563 fields that were converted from arable land to grassland from 2001 to 2003 and 2005 to 2015 ("arable land conversion") and 17.4 km^2 of communal grasslands where extensive grazing was encouraged from 2003 to 2013 ("communal grasslands").

2.4. Annual habitat mapping

2.4.1. Generating the reference dataset

Dataset 1 was generated from field data and historical aerial photographs to train and test the habitat classification models in 1984 and 2022 for the CCDC and diachronic methods. While the time difference between the date of the Landsat images and that of the reference data must be as small as possible for the diachronic method, this is not required for CCDC. Consequently, Dataset 1 contained all points collected from 1984 to 2022, regardless of the date.

A three-step workflow was performed to extract reference points from field data. First, all field data were converted to the EUNIS classification system at level 1 (Davies et al., 2004), which describes seven major habitat types (Table 1 in supplementary material B). Specifically, we used the guide of Delassus et al. (2014) for the regional classification of vegetation, the French Habref reference guide (Clair et al., 2017) for the CORINE Biotopes classification systems, the crosswalk table of Chytrý et al. (2020) for the EUNIS 2020 classification system, and the two crosswalk tables of Buck et al. (2015) and the European Environmental Agency (EEA, 2014) to convert the LUCAS classification system to CORINE Land cover and then to the EUNIS classification system. For the LPIS data, all crop types were assigned to habitat I (i.e., *Regularly or recently cultivated agricultural, horticultural and domestic habitats*), except for old pastures, which were assigned to habitat E (i.e., *Grasslands and lands dominated by forbs, mosses or lichens*). The fields in the "arable land conversion" and "communal grasslands" layers were also assigned to habitat E.

In the second step, the EUNIS classification system was adjusted for habitats C (i.e., *Inland surface waters*) and J (*Constructed, industrial and other artificial habitats*), since they included spectrally heterogeneous habitats. More specifically, we merged habitats C1 (i.e., *Surface standing waters*) and J5 (i.e., *Highly artificial manmade waters and associated structures*), since they have similar spectral signatures. In addition, habitat C3 (i.e., *Littoral zone of inland surface waterbodies*) was considered separately because its spectral signature differs from that of surface water, and habitat C2 (i.e., *Surface running waters*) was excluded because it was undetectable at the study site due to Landsat's low spatial resolution. Thus, the final classification system contained eight habitat types:

- *A – Marine habitats*
- *B – Coastal habitats*
- *C1/J5 – Natural permanent surface waters* and *Artificial permanent surface waterbodies*

Table 2
Summary and description of field vegetation data used in the study. LULC: land use and land cover.

Name	Type	Format	Approximate scale/ accuracy	Nomenclature	Years	Source
Vegetation maps of natural reserves	Vegetation	Polygons	1:5 000	EUNIS 2004 (Davies et al., 2004) Regional classification of vegetation (Delassus et al., 2014)	2006, 2009, 2012, 2013, 2015	INPN (Robert and Brosseau, 2022)
Natura 2000 habitat map	Vegetation	Polygons	1:15 000	CORINE Biotopes (Devillers et al., 1991)	2001–2005	Local managers
Vegetation relevés	Vegetation	Points	1 m	EUNIS 2020 (Chytrý et al., 2020)	2001, 2002, 2004, 2005, 2006, 2014, 2015	VegFrance (Bonis and Bouzillé, 2012) and local managers
LPIS	LULC	Polygons	1: 5 000	LPIS	2007, 2010, 2015	IGN (https://geoservices.ign.fr/rpg)
LUCAS	LULC	Points	5 m	LUCAS	2006, 2012, 2018	ESDAC (https://esdac.jrc.ec.europa.eu/projects/lucas)
Arable land conversion	LULC	Polygons	1:5 000	–	2001–2003, 2005–2015	Local managers
Communal grasslands	LULC	Polygons	1:5 000	–	2003–2013	Local managers

- *C3 – Littoral zone of inland surface waterbodies*
- *E – Grasslands and lands dominated by forbs, mosses or lichens*
- *G – Woodland, forest and other wooded land*
- *I – Regularly or recently cultivated agricultural, horticultural and domestic habitats*
- *J – Constructed, industrial and other artificial habitats*

In the third step, reference points were visually extracted from field GIS layers so that they lay entirely within a Landsat pixel (30 × 30 m). Field data in polygon format were overlaid on a vector grid of Landsat image pixel contours to automatically select all pixels that lay completely within the polygons. For field data in point format, the reference data corresponded to points manually identified in vegetation patches that lay entirely within a Landsat pixel. The vegetation patches had been previously delineated via visual interpretation of aerial photographs taken on the date closest to that on which the field data had been collected. A total of 100 reference points, corresponding to the approximate number of available points for the least represented habitats (A, B, and C3), were randomly selected per habitat per year to balance Dataset 1.

Due the lack of field data before 2001 and after 2016, Dataset 1 was supplemented with points obtained from visual interpretation of historical (1984, 1990, and 1997) and recent (2022) aerial photographs to cover the entire period. For each year, 100 reference points per EUNIS habitat were selected within all vegetation patches that lay completely within a Landsat pixel. The relatively low quality of the historical aerial photographs prevented unambiguous identification of habitats B (i.e., *Coastal habitats*) and C3. For these habitats, the 1990 and 1997 reference points were discarded since they were optional for CCDC and not used for the diachronic method. Conversely, the 1984 reference points were retained since they were required for the diachronic method (Table 3). Ultimately, Dataset 1 contained 4 200 points collected from 1984–2022 (Table 3) that were randomly divided per year and habitat into training (80 %) and testing (20 %) samples.

2.4.2. Continuous change detection and classification

2.4.2.1. Harmonic regression. A continuous simulated time-series for 1984–2022 was produced for each Landsat spectral band and index (Table 1) using a harmonic regression model (Zhu and Woodcock, 2014b). Specifically, the least absolute shrinkage and selection operator (LASSO) was selected as regression type, since it rarely overfits (Tibshirani, 1996) and remains robust when using infrequent observations (Zhu et al., 2015). The Google Earth Engine CCDC application programming interface includes two versions with slightly different default parameter values (Arévalo et al., 2020). During the preliminary calibration step, we tested the default values of these two versions for all parameters and retained the best values based on a visual interpretation of the results (Table 4).

For each pixel, the model was fitted to a stable historical period at the beginning of the time series. The model was then fitted iteratively to the next set of clear Landsat observations until the fitted values differed significantly from the values observed on five consecutive dates, which indicated a potential change in natural habitat. When a break was detected, a new temporal segment was begun using a new harmonic regression model (Fig. 3). This process was then repeated until the end of the time series. The *TMask* multitemporal algorithm (Zhu and Woodcock, 2014b) was applied throughout the process to detect and discard any noisy Landsat observations previously missed by the *CFMask* algorithm.

A total of 15 CCDC algorithm coefficients and derivatives characterizing each temporal segment per pixel were calculated for each spectral band and index (Table 5).

2.4.2.2. Random forest classification. CCDC algorithm coefficients and derivatives of the seven Landsat bands and eight indices, as well as the three environmental variables, were used as input variables for classifying habitats. The random forest (RF) classifier can manage many input variables from different sources and has little sensitivity to outliers or over-fitting (Belgiu and Drăguţ, 2016). RF classification was performed using the GEE *ee.Classifier.smileRandomForest* function, using all default parameters, except for the maximum number of trees, which was increased to 500. All training samples collected for 1984–2022 were used to calibrate the classifier. Although the CCDC algorithm could have generated habitat maps for any year of the study period, we generated habitat maps only for 1984 and 2022 to detect changes over the longest time span in order to compare its predictions to those of the traditional

Table 4
Harmonic regression parameters used in the continuous change detection and classification and set in the scripts of the Google Earth Engine CCDC application programming interface. Exponent letters [a] and [b] indicate respectively default values from version 1 * and 2 ** of the application programming interface.

Parameter	Meaning	Value
breakpointBands	The name or index of the bands used to detect change	All[.ab]
tmaskBands	The name or index of the bands used to detect clouds and noise iteratively (*TMask*)	Green, SWIR2[.ab]
MinObs	Moving window size used to detect breaks	5[.a]
Seg	Maximum number of temporal segments in the entire time-series	6[.ab]
Lambda	Penalty parameter for LASSO regression	0.005[.a]
ChiSquareProbability	Chi-square probability threshold for break detection	0.99.[b]
MinNumOfYearsScaler	Factor of minimum number of years to apply a new regression model	1.33[.ab]
MaxIterations	Maximum number of runs for LASSO regression convergence	10 000[.b]

* https://code.earthengine.google.com/?scriptPath=users%2Fparevalo_bu%2Fgee-ccdc-tools%3AAPPS%2Fsubmit_ccdc and https://code.earthengine.google.com/?scriptPath=users%2Fparevalo_bu%2Fgee-ccdc-tools%3AccdcUtilities%2Finputs.js.
* https://code.earthengine.google.com/?scriptPath=users%2Fparevalo_bu%2Fgee-ccdc-tools%3AAPPS%2Ftstools_advanced.

Table 3
Number of reference points per year and EUNIS habitat type (level 1). Gray cells indicate reference points for 1984–1997 and 2022 that were collected from visual interpretation of historical aerial photographs and recent aerial photographs, respectively, due to the lack of field reference data before 2001 and after 2016.

EUNIS habitat type	Years										
	1984	1990	1997	2001	2002	2005	2006	2015	2016	2022	All
A	100	100	–	–	–	–	100	100	–	100	500
B	100	–	–	–	100	–	100	–	–	100	400
C1/J5	100	100	100	–	100	–	–	–	100	100	600
C3	100	–	–	100	100	–	–	–	–	100	400
E	100	100	100	100	–	100	100	–	–	100	700
G	100	100	100	100	–	–	–	–	–	100	500
I	100	100	100	100	–	–	–	–	–	100	500
J	100	100	100	–	100	–	100	–	–	100	700
All	800	600	500	400	400	100	400	100	100	800	4200

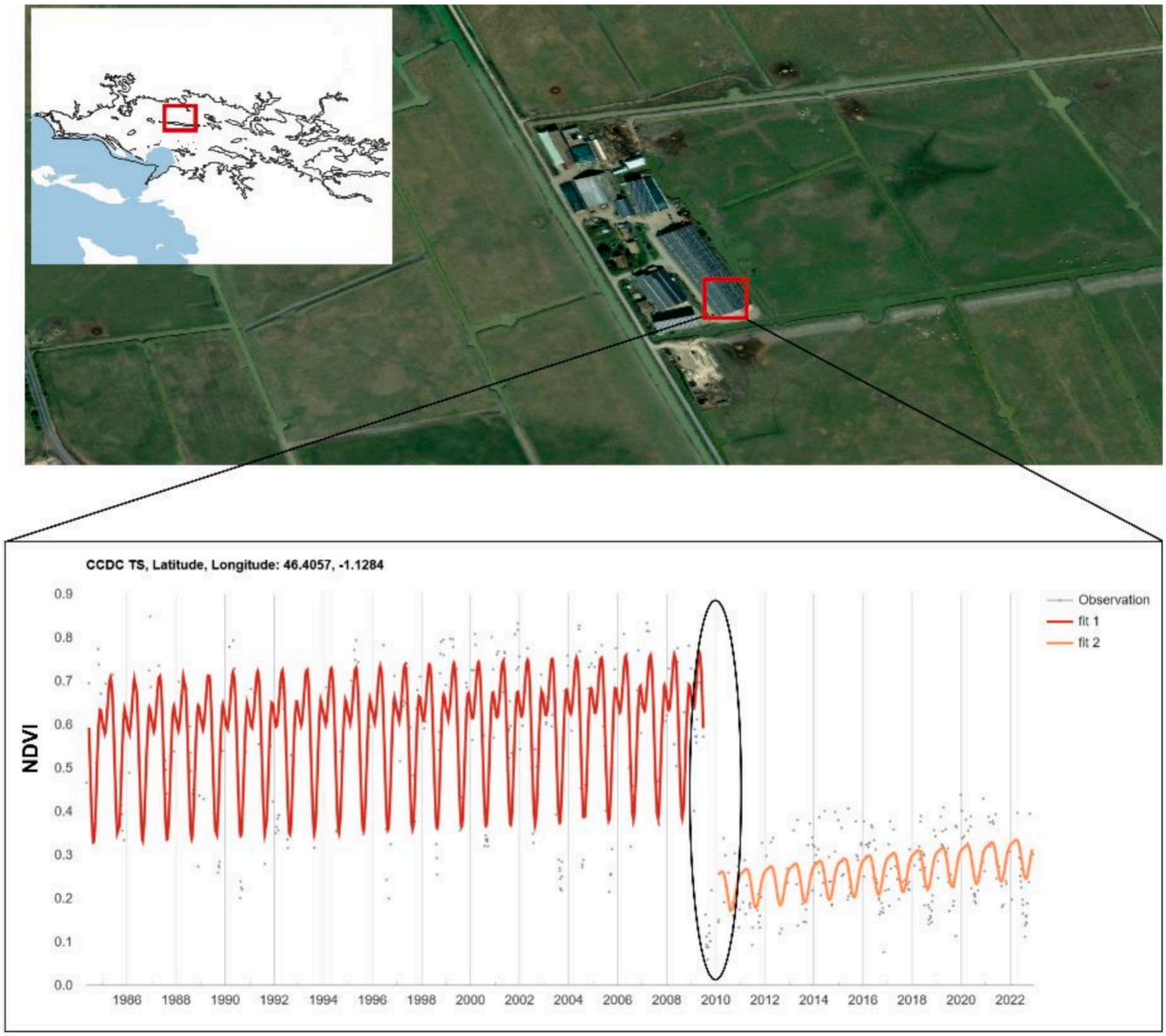

Fig. 3. Example of a one-pixel NDVI time-series extracted from the Landsat archive for the Marais Poitevin from 1984–2022. The fits in the colored lines indicate temporal segments detected by the continuous change detection and classification (CCDC) algorithm. A change in color indicates a change in land cover/land use. The red segment corresponds to the NDVI signal from grasslands until a break in ca. 2010 (black ellipse), when grasslands were converted to built-up areas (orange segment).

post-classification method. The two annual habitat classifications may have contained a few no-value (NA) pixels due to initializing harmonic regression at the beginning of the period or immediately after a break (e.g., black ellipse, Fig. 3). These NA pixels were assigned to the dominant habitat type using a modal filter with a 5 × 5 sliding window.

2.4.3. Traditional classification

2.4.3.1. Selection of cloud-free Landsat images. Cloud-free images were first automatically selected for 1984 and 2022 using a cloud-cover criterion (0 %) and then visually checked to discard images that covered only part of the site and/or contained haze or residual noise. For 1984, two L5 TM images (18 Aug, path/row 201/28; 30 Oct, path/row 200/28) were mosaicked to obtain one early-autumn composite image. Specifically, pixels of the most recent image were used first in the mosaic, and missing pixels were filled in with pixels of the oldest image using the Google Earth Engine *ee.ImageCollection.mosaic()* function. For 2022, four L8-9 OLI/TIRS images were selected to obtain one mid-summer composite (10 Jul, path/row 201/28; 11 Jul, path/row 200/28) and one late-summer composite (20 Sep, path/row 201/28; 21 Sep, path/row 200/28). The eight spectral indices were then calculated for each composite (Table 1).

2.4.3.2. Random forest classification. RF classification was performed for 1984 and 2022 separately using spectral bands and spectral indices derived from each year's composites, as well as environmental variables. RF classifications were performed using the same GEE function and parameters used for CCDC, but each RF classifier was calibrated using only training samples collected for the corresponding year. This method generated two habitat maps: one for 1984 from the first RF classifier and one for 2022 from the second RF classifier.

Table 5
Continuous change detection and classification (CCDC) outputs used as predictor variables for random forest classification of natural habitats. The acronyms correspond to those defined in the Google Earth Engine CCDC application programming interface (Arévalo et al., 2020). See Zhu and Woodcock (2014) for more detailed description of each coefficient and derivative.

CCDC output type	Acronym	Description
Coefficients	INTP	Intercept: Intercept of the time series. Mean reflectance for spectral bands or mean value for spectral indices and indicators.
	SLP	Slope: Long-term trend of the time series
	SIN	Sine and cosine: Harmonic coefficients for intra-annual change
	COS	
	SIN2	Sine and cosine: Harmonic coefficients for intra-annual bimodal change
	COS2	
	SIN3	Sine and cosine: Harmonic coefficients for intra-annual trimodal change
	COS3	
	RMSE	Root mean square error: The error between the observed and CCDC fitting values. Corresponds to non-seasonal variability.
Derivatives	AMPLITUDE	Magnitude of the time series. Corresponds to seasonal variability. Derived from COS and SIN.
	PHASE	Phenological timing of the time series. Derived from COS and SIN.
	AMPLITUDE2	Bimodal magnitude of the time series. Derived from COS2 and SIN2.
	PHASE2	Bimodal phenological timing of the time series. Derived from COS2 and SIN2.
	AMPLITUDE3	Trimodal magnitude of the time series. Derived from COS3 and SIN3.
	PHASE3	Trimodal phenological timing of the time series. Derived from COS3 and SIN3.

2.5. Change detection

The change detection analysis described and compared wetland dynamics between 1984 and 2022 and then compared continuous and post-classification change detection methods. A two-step procedure was applied in parallel for each method. First, wetlands in annual habitat maps 1984 and 2022 were simplified into "existing wetland" (habitats A, B, C3, E, and G) or "damaged wetland" (habitats C1/J5, I, and J) based on Rapinel et al. (2018). In the second step, the wetland change map was derived by subtracting the 2022 two-class map from the 1984 map. Four classes were identified from the change map: (i) "wetland loss", which described a change from existing to damaged wetland; (ii) "wetland gain", which described a change from damaged to existing wetland; (iii) "stable existing wetland", which described stability of an existing wetland; and (iv) "stable damaged wetland", which described stability of a damaged wetland.

2.6. Accuracy assessment

The accuracy of the 1984 and 2022 habitat classifications was determined for the two methods using the same testing sample for the given year (i.e., 1984 or 2022) extracted from Dataset 1. For each date (1984 or 2022), we calculated a confusion matrix, the overall accuracy, user's accuracy (UA), and producer's accuracy (PA) per habitat (Tables S1–S4 in supplementary material A).

The unbiased accuracy and estimated area of the wetland-state change map were calculated for the two methods according to Olofsson et al. (2014), which provided the magnitude of the classification errors needed to adjust the area estimator. To this end, stratified validation sampling (Dataset 2) was performed based on the change map derived from continuous change detection. Specifically, the number of samples per class of change was defined as a function of the expected standard deviation of overall and class-specific accuracy. First, the expected standard deviation of overall accuracy was set at 0.015 to achieve a trade-off between the required minimum of 50 samples per class and a rapid strategy for visual interpretation. The expected standard deviation for each class was then set to be higher for under-represented classes: 0.2, 0.3, 0.4, and 0.5 for "stable damaged wetland", "stable existing wetland", "wetland loss", and "wetland gain", respectively. A total of 326 validation samples were automatically assigned (i.e., 62, 54, 101, and 109 for "wetland loss", "wetland gain", "stable existing wetland", and "stable damaged wetland", respectively). Each validation sample included visual interpretation of aerial photographs for 1984 and 2022 and very high spatial resolution satellite imagery available in Google Earth Pro, supplemented with Landsat NDVI time series supplied by the API CCDC visualizer (Arévalo et al., 2020). The unbiased overall accuracy, UA, PA, and estimated area for each change detection class were calculated using the R package *mapaccuracy* (Costa, 2022).

3. Results

3.1. Habitat map accuracy

While the overall accuracy of habitat maps derived from CCDC and post-classification was high for both years (Table 6), that of post-classification was higher for 1984 (0.93 and 0.86, respectively) but was much lower for 2022 (0.75 and 0.91, respectively). Accuracies for habitat types A, B, C1/J5, G, and J were high (UA and PA $>$ 0.75). Conversely, for 2022, accuracies for habitat E were moderate for CCDC (UA = 0.61 and PA = 1.00) and low for post-classification (UA = 0.45 and PA = 0.75). Similarly, for 1984, accuracies for habitat I were high for CCDC (UA = 1.00 and PA = 0.95) and moderate for post-classification (UA = 0.66 and PA = 0.95). For 2022, accuracies for habitat C3 were low for CCDC (UA = 1.00 and PA = 0.40) and even lower for post-classification (UA = 80.20 and PA = 0.05).

The post-classification accuracy has varied strongly (0.93 in 1984 and 0.75 in 2022), while the CCDC accuracy has remained constant over time (0.86 in 1984 and 0.91 in 2022). This could be explained by the characteristics of the two classification methods: the first is based on the discriminant capacity of the pair of composite images used, which varied from one year to another, while the second is based on a sequence of images, which makes it more stable over time. The analysis of the confusion matrix for habitat types in 2022 derived from the post-classification change detection (Table S2 in Supplementary Material A) showed that most classification errors occurred between E and C3 habitats, and to a lesser extent between I and E habitats, highlighting that the dates of the Landsat images used (mid- and late-summer composites) were not optimal for discriminating these habitats in 2022. In contrast, the date of the image composite (early autumn) was more appropriate for discriminating these habitats in 1984 (Table S1 in Supplementary Material A). The variability in the accuracy of the post-

Table 6
User's accuracy (UA) and producer's accuracy (PA) of habitat maps in 1984 and 2022 obtained using continuous change detection and classification (CCDC) and post-classification. Bold text indicates the highest accuracy per year and habitat.

	1984 CCDC		1984 Post-classification		2022 CCDC		2022 Post-classification	
EUNIS habitat types	UA	PA	UA	PA	UA	PA	UA	PA
A	0.90	0.90	**1.00**	**0.95**	**1.00**	**0.95**	0.74	0.85
B	0.85	0.85	**1.00**	**1.00**	1.00	**1.00**	1.00	0.75
C1/J5	1.00	1.00	1.00	1.00	1.00	**1.00**	1.00	0.95
C3	1.00	0.40	1.00	**0.91**	**1.00**	**0.40**	0.20	0.05
E	0.73	**0.95**	**0.80**	0.84	**0.61**	**1.00**	0.45	0.75
G	0.80	**1.00**	**1.00**	0.83	**1.00**	1.00	0.91	1.00
I	**0.88**	0.75	0.80	**0.89**	**1.00**	0.95	0.66	0.95
J	**0.83**	1.00	0.81	1.00	0.95	**1.00**	**1.00**	0.70
Overall Accuracy (%)	0.86		**0.93**		**0.91**		0.75	

classification method explained why the accuracy of this method was slightly higher than that of the CCDC in 1984, whereas the accuracy of the CCDC was significantly higher than that of the post-classification in 2022.

3.2. Change detection accuracy

The unbiased accuracies of the wetland change maps (Table 7) calculated using the method of Olofsson et al. (2014) indicated a low uncertainty in the accuracy estimate, with a 95 % confidence interval between 0.01 and 0.08. Continuous change detection outperformed post-classification change detection (overall accuracy = 0.86 ± 0.02 and 0.51 ± 0.03, respectively), highlighting the value of the former method based on the analysis of temporal profiles and the main limitation of the latter method due to the sum of the classification errors. Specifically, stable existing wetlands were accurately classified using continuous change detection (UA 0.83–0.90 and PA 0.90–0.96) and less accurately using post-classification change detection (UA 0.58–0.69 and PA 0.26–0.81), whereas wetland loss and gain were classified with moderate accuracy using continuous change detection (UA 0.48–0.93 and PA 0.56–0.62) and very low accuracy using post-classification change detection (UA 0.21–0.39 and 0.19–0.58).

Applying the two methods to detect change between 1984 and 2022 using aerial photography for areas dominated by two change classes in the Marais Poitevin (i.e. stable degraded wetlands vs. wetland loss due to conversion of grasslands to cropland) indicated that continuous change detection accurately detected both classes, unlike post-classification change detection (Fig. 4).

3.3. Areas of wetland change

Areas of wetland change between 1984 and 2022 mapped using continuous change detection (Table 8) highlighted that wetland state changed over ca. 20 % of the Marais Poitevin. Wetland loss was much larger than wetland gain (ca. 18 % and 2 %, respectively). Damaged wetlands covered the largest area of the Marais Poitevin in 2022. Conversely, the percentage of existing wetland area in 1984 decreased by 16 percentage points to cover less than half (ca. 41 %) of the Marais Poitevin in 2022.

Locations of wetland changes between 1984 and 2022 using continuous change detection varied (Fig. 5). Most stable existing wetlands were located inside the Natura 2000 protected site, while stable degraded wetlands were located outside of it. Wetland losses were concentrated mainly in the east-central part of the Marais Poitevin within the large areas of stable degraded wetlands. Conversely, most of the wetland gains were scattered throughout the Natura 2000 site.

Analysis of the drivers of wetland change revealed that wetland loss was due mainly to conversion to arable land (ca. 95 %) and, to a lesser extent, constructed habitats and creation of artificial waterbodies (ca. 4 % and 1 % of the area of wetland loss, respectively). Conversely, wetland gain was due to both natural (e.g., sediment accumulation) and human drivers (e.g., conversion, abandoning farming practices). More specifically, most wetland gain was due to grassland expansion (ca. 80 %), followed by an increase in habitat A (i.e., *Marine habitats*) (ca. 11 %) from 1984 to 2022. To a lesser extent, the area of habitat C3 increased by ca. 5 %, followed by that of habitats G (ca. 4 %) and B (i.e., *Coastal habitats*) (ca. 2 %). We highlighted examples of wetland loss (Fig. 6) and gain (Fig. 7) due to these drivers of change.

Table 7
User's accuracy (UA) and producer's accuracy (PA) of continuous and post-classification change detection using the method of Olofsson et al. (2014).

	Continuous		Post-classification	
	UA	PA	UA	PA
Wetland loss	0.93 ± 0.04	0.56 ± 0.05	0.39 ± 0.05	0.58 ± 0.05
Wetland gain	0.48 ± 0.08	0.62 ± 0.08	0.21 ± 0.08	0.19 ± 0.07
Stable existing wetland	0.83 ± 0.04	0.96 ± 0.01	0.58 ± 0.04	0.81 ± 0.03
Stable damaged wetland	0.90 ± 0.03	0.90 ± 0.02	0.69 ± 0.07	0.26 ± 0.03
Overall accuracy (%)	0.86 ± 0.02		0.51 ± 0.03	

4. Discussion

4.1. Continuous vs. post-classification change detection methods

This study highlights the value of using continuous change detection rather than post-classification change detection to detect changes in wetlands over a 39-year interval. The accuracy of the annual maps obtained using continuous change detection was satisfactory and similar to that obtained using post-classification change detection. Specifically, the overall accuracy of the annual habitat maps obtained with continuous change detection was high (> 0.85) and similar to that obtained for coastal wetlands in China (He et al., 2022; Peng et al., 2021; Wang et al., 2023), Bangladesh (Awty-Carroll et al., 2019), and the USA (Yang et al., 2022), confirming the generic nature of the CCDC algorithm for coastal wetlands. The largest classification errors were for grassland habitats (E), which are the most difficult to classify (Liu et al., 2020; Xie et al., 2022). Some of them were classified as habitat C3 (i.e., *Littoral zone of inland surface waterbodies*), since the physiognomy of some unmanaged wet grasslands can resemble that of C3 vegetation, making it difficult to distinguish the two habitats.

However, accuracy was higher for the change maps obtained using continuous change detection than using post-classification change detection. This could have been due to the cumulative misclassification of the two annual habitat maps (7 % in 1984 and 25 % in 2022) obtained using the latter, which inevitably led to the detection of false changes (Fuller et al., 2003; Gómez et al., 2016). The most frequent confusion was between cropland (I) and grassland (E) habitats (Fig. 4, Tables S1–S2 in supplementary material A), which resulted in inadequate characterization of changes in wetland conservation.

Continuous change detection avoided most of these misclassification errors, making it possible to classify the temporal profile of the entire study period by using all Landsat archive images, including partially cloudy images and those acquired by the ETM+SLC-off sensor, totaling several hundred clear observations per pixel (Figure S1 in supplementary material A). Another advantage of continuous change detection is that it uses the temporal profile of the entire study period to make predictions for the years selected (here, 1984 and 2022) using asynchronous reference data with a single classifier. In this way, all field data collected during the study period (2000–2010) were used to classify wetlands before (1984) and after (2022) reference data had been collected.

These two advantages explain the much higher overall accuracy of the wetland change map obtained using continuous change detection (0.86) than that obtained using post-classification change detection (0.51). However, accuracy was lower for the maps of wetland change (i.e., "wetland gain" and "wetland loss") than for the maps of wetland stability (i.e., "stable existing wetland" and "stable damaged wetland") (Table S5 in supplementary material A). Several studies achieved similar results when using the CCDC algorithm and Landsat archive images for urban (Xie et al., 2022), forest (Chen et al., 2021), or wetland (Yang et al., 2022) ecosystems. In agreement with Chen et al. (2021), the PA errors could have been due to the few clear Landsat observations at the beginning of the time series, which resulted in a poor fit of the harmonic regression model that led to false break detection when the number of observations increased. The UA errors could have occurred because the CCDC algorithm did not detect a break in the time series, or detected a break, but the magnitude of the change was lower than the detection

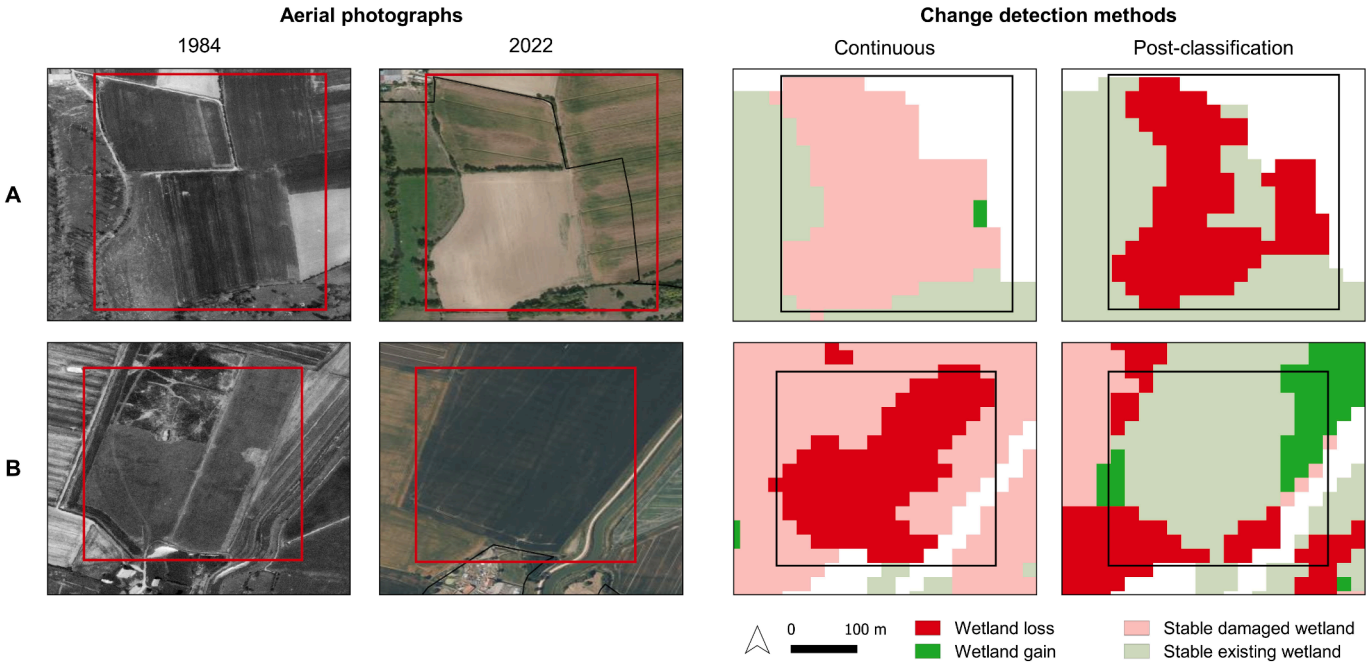

Fig. 4. Comparison of continuous and post-classification change detection between 1984 and 2022 for two areas of the Marais Poitevin: area A (46° 19′ N, 0° 33′ W), with a stable degraded wetland due to the presence of arable land, and area B (46° 23′ N, 1° 10′ W), with wetland loss, since grassland in 1984 had been converted to arable land by 2022. A 3 × 3 modal filter was applied to the change maps in post-processing to reduce the salt-and-pepper effect. Source of aerial photographs: French National Geographic Institute (IGN).

Table 8
Unbiased estimate of wetland area (in ha and percentage of total site area) with 95 % confidence intervals for the four wetland-change classes between 1984 and 2022 using continuous change detection and classification.

Item	Wetland loss	Wetland gain	Stable existing wetland	Stable damaged wetland
Unbiased area estimate (ha)	18 286 ± 3 365	2 234 ± 1 248	40 808 ± 3 492	37 659 ± 2 888
Percentage of total site area	18.5 ± 1.7	2.2 ± 0.6	41.2 ± 1.8	38.0 ± 1.5

threshold (*ChiSquareProbability*).

This study is the first to highlight the higher performance of the continuous method over the post-classification method for change detection in wetlands. Although these two methods are among the most popular (Gómez et al., 2016; Pasquarella et al., 2022) other ones have recently shown interest in wetland monitoring, such as the Detection and Characterisation of Coastal Tidal Wetland Change (DECODE) (Yang et al., 2022) or the Domain Adaptive and Interactive Differential Attention Network (DA-IDANet) (Ji et al., 2024) and deserve to be further compared. In addition, our study which was applied to a small coastal marsh of about 1000 km^2 in Europe should be further tested on other types of wetlands and in other geographical areas to assess the sensitivity of these methods to wetland dynamics and to field and

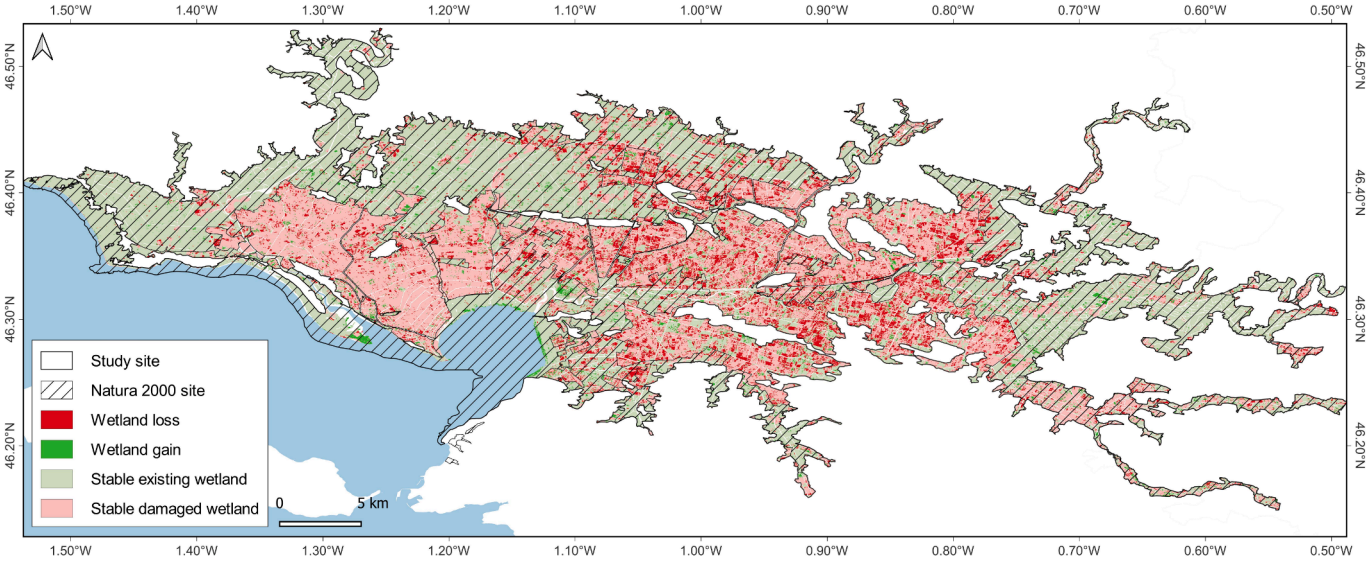

Fig. 5. Wetland changes detected in the Marais Poitevin site between 1984 and 2022 using continuous change detection.

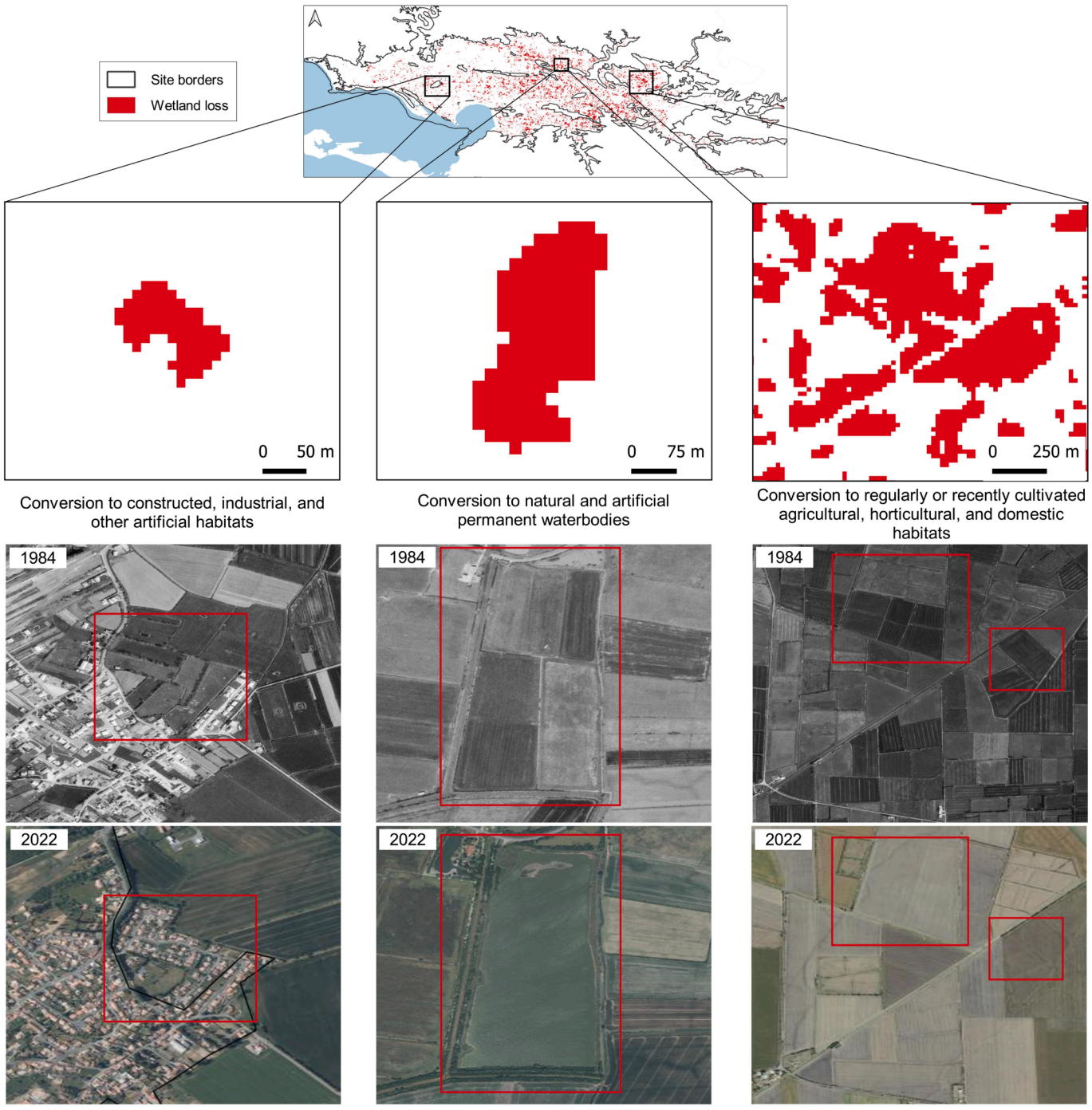

Fig. 6. Examples of wetland loss between 1984 and 2022 due to urbanization (left), conversion to natural and artificial waterbodies (middle), and conversion to arable land (right) derived from continuous change detection, and aerial photographs (IGN). A 3 × 3 modal filter was applied to the change map in post-processing to reduce the salt-and-pepper effect.

satellite data availability.

4.2. Landsat archive and CCDC algorithm for monitoring wetlands

This study confirmed the value of using Landsat archive images to monitor wetlands over the long term (Demarquet et al., 2023). While the spatial resolution of Landsat images limited the ability to detect changes in linear habitats, such as in habitats C3 or G, it was sufficient for detecting the main changes of human origin (e.g., urban sprawl, agricultural intensification) or natural origin (e.g., coastal sedimentation). In addition, the cloud and outlier masks implemented in the CCDC algorithm yielded many clear Landsat observations per pixel (i.e., 238–760), despite the high frequency of cloud cover in Western Europe. However, the number of clear observations was significantly lower over the sea and lakes, as well as over arable land, suggesting an over-detection of shadows on water and bare soil (Figure S1 in supplementary material A). This problem, recognized by the authors of *CFmask* (Foga et al., 2017) and *Tmask* (Zhu and Woodcock, 2014b), was not an issue in the present study, since the minimum number of clear observations (238) was sufficient to detect habitat changes. However, this could be an issue when monitoring wetlands at sites with high cloud cover and/or frequent flooding.

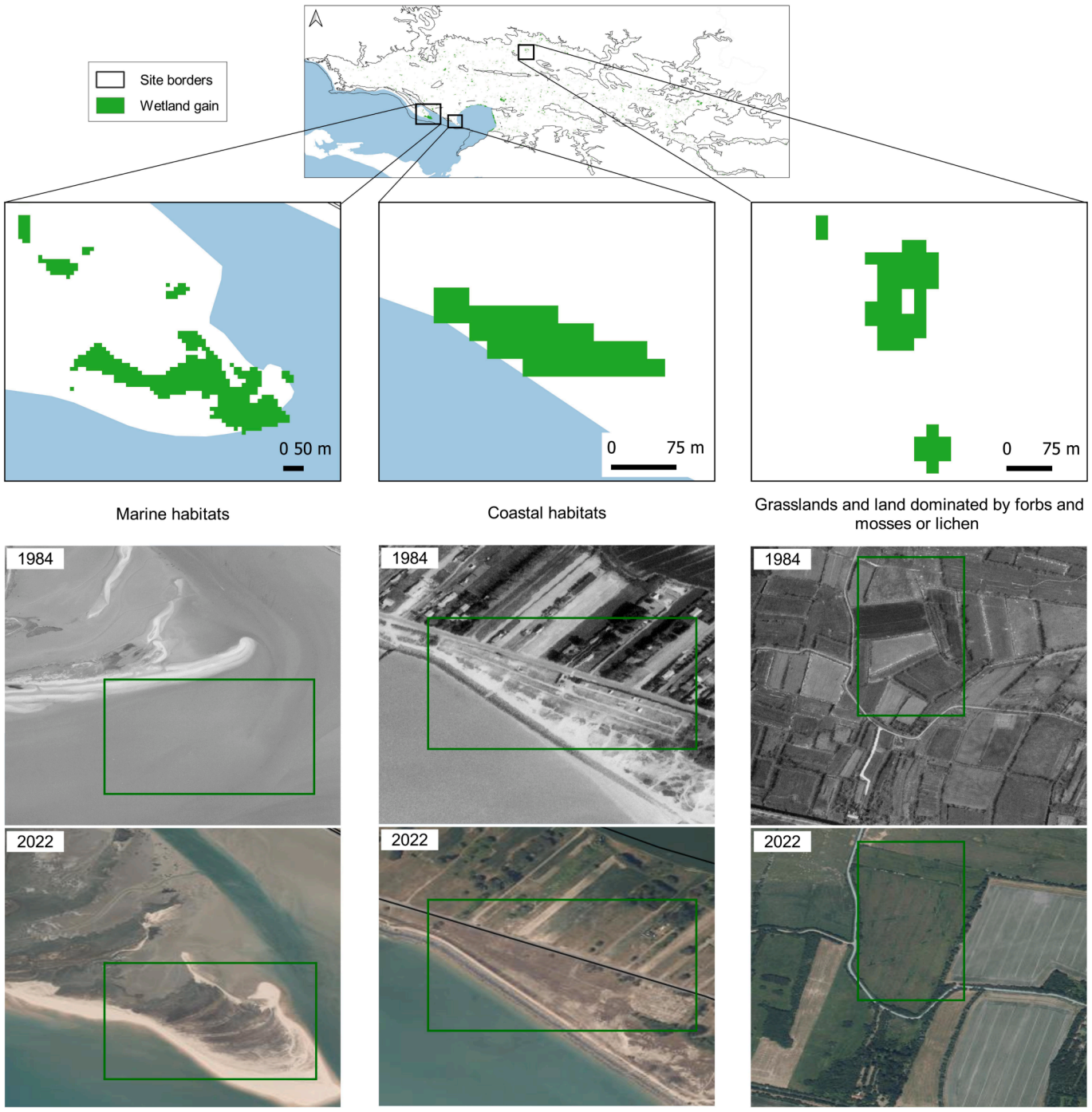

Fig. 7. Examples of wetland gain between 1984 and 2022 due to natural coastal sedimentation (left); conversion of constructed, industrial, and other artificial habitats to coastal habitats (middle); and conversion of arable land to grasslands (right) derived from continuous change detection, and aerial photographs (IGN). A 3 × 3 modal filter was applied to the change map in post-processing to reduce the salt-and-pepper effect.

The CCDC algorithm was able to detect abrupt habitat changes by identifying significant breaks in the temporal profile. For this reason, parameterization of the CCDC algorithm is crucial, in particular (i) the minimum number of consecutive observations for break detection (*minObs*) and (ii) the threshold value for break detection (*ChiSquareProbability*) (Pasquarella et al., 2022). We set the default value of the *ChiSquareProbability* parameter to 0.99, as Yang et al. (2022) did for coastal wetlands in the USA. Conversely, the default values of parameters *minObs* and *lambda* were suitable for our study site, while Yang et al. (2022) increased *minObs* to 6 and Awty-Carroll et al. (2019) increased *lambda* to 1 when monitoring mangroves. Thus, there seems to be no consensus on parameter values, since the CCDC algorithm must be parameterized for the structural and functional characteristics of the area studied. In our study the classification accuracy could also be improved using a hyper tuning procedure of the CCDC parameters as demonstrated in Yang et al. (2022) instead of using default values.

The method applied in this study was able to assess changes in wetland state based on a map of the main habitat types (Rapinel et al., 2018). However, it was unable to assess the natural vs. artificial character of certain habitats, especially natural (habitat C1) and artificial (habitat J5) waterbodies, as well as wooded areas (habitat G), which indicate wetland state. We considered habitat C1/J5 a poor indicator of

wetland state, since many of the waterbodies were waterfowl-hunting ponds created in the 1980s (Duncan et al., 1999). Future studies could analyze changes in wetland state in greater detail by detecting progressive changes within the same habitat (e.g., eutrophication of grasslands) based on recent continuous change detection methods, such as object-based continuous monitoring of land disturbances (OB-COLD) (Ye et al., 2023), DECODE (Yang et al., 2022), or new deep learning methods (Huang et al., 2022; Ji et al., 2024; Liu et al., 2022; Sun et al., 2021).

CCDC has been successfully and widely used to map land cover and land cover change at regional scale (Friedl et al., 2022). Our study confirmed the value of the CCDC approach by showing its effectiveness in detecting habitat change within a Ramsar wetland compared to the traditional method. However, in our study, a large number of Landsat images were available, which is not always the case: for example, in some regions of the world, such as Siberia, the Pacific Islands or West Africa, the number of clear observations per year is insufficient (<4) to fit robust CCDC models (Zhang et al., 2022). In this case, the traditional method based on composites using available historical Landsat data is an option (Potapov et al., 2012). In addition, we had a large number of high-quality field observations, which is essential to train high-quality classification models (Friedl et al., 2022). The availability of new crowdsourced data, such as the GeoWiki Global Land Cover and Land Use reference dataset (Fritz et al., 2017), which contains over 150,000 100-m grid cells, can partially compensate for the lack of field observations in wetlands.

4.3. Continuous change detection for conservation

Results of the present study agree with those of previous studies that have highlighted the degradation of wetland state in the Marais Poitevin due to conversion of grasslands to cropland (Duncan et al., 1999; Godet and Thomas, 2013) and increasing urbanization in the littoral zone (Pouzet et al., 2015) since 1950. In addition, wetland loss at this site was also related to the construction of artificial waterbodies, such as hunting ponds (Duncan et al., 1999) and wastewater treatment ponds. Conversely, wetland gain, although small, was due mainly to conversion of arable land to grassland, which highlights the conservation efforts of site managers as well as the agri-environmental incentives offered to farmers under the CAP (Petit et al., 2022). The wetland gain of shore meadows was due to sediment accumulation caused by construction of dykes at the entrance of the marsh (Regnauld et al., 2015).

More generally, continuous change detection based on dense Landsat time-series has enabled standardized (i.e., same data and method) long-term monitoring of wetland ecosystem structure, which is essential for biodiversity (Skidmore et al., 2021). This method overcomes the biases currently encountered in Ramsar (Davidson et al., 2019) or the European Union's Habitat Directive (Delbosc et al., 2021), whose monitoring has not yet been standardized (e.g. changes in field observers, different data sources and methods). In addition, combining the free Landsat archive (Wulder et al., 2022) and CCDC API (Arévalo et al., 2020) with an intuitive graphical interface on the GEE platform makes this method simple to use by non-specialists in remote sensing such as wetland managers or policy makers seeking to assess the impact of restoration measures or wetland health indicators, including those in developing countries.

5. Conclusion

This study, focused on a coastal marsh in France, highlights that while continuous change detection and post-classification change detection had similar overall accuracy, the wetland change maps of the former between 1984 and 2022 were much more accurate. We recommend further testing continuous change detection to detect changes in wetlands, especially since APIs are now freely available in cloud computing, which makes processing straightforward. Future research will focus on detecting changes, including subtle ones, in other wetland types and geographical areas, comparing CCDC with various change detection methods, including deep learning algorithms. This will support the monitoring of wetland health to meet conservation plans, such as Ramsar reporting.

CRediT authorship contribution statement

Quentin Demarquet: Writing – original draft, Visualization, Validation, Formal analysis, Data curation. **Sébastien Rapinel:** Writing – original draft, Resources, Conceptualization. **Olivier Gore:** Writing – review & editing, Resources. **Simon Dufour:** Writing – review & editing. **Laurence Hubert-Moy:** Writing – original draft, Supervision, Conceptualization.

Declaration of competing interest

The authors declare that they have no known competing financial interests or personal relationships that could have appeared to influence the work reported in this paper.

Data availability

Data will be made available on request.

Acknowledgements

Quentin Demarquet received a Ph.D. grant (2021-2024) from the French Ministry of Higher Education, Research and Innovation. The authors acknowledge the U.S. Geological Survey for making the Landsat data freely available.

Appendix A. Supplementary data

Supplementary data to this article can be found online at https://doi.org/10.1016/j.jag.2024.104142.

References

Arévalo, P., Bullock, E.L., Woodcock, C.E., Olofsson, P., 2020. A suite of tools for continuous land change monitoring in google earth engine. Frontiers in Climate 2.
Awty-Carroll, K., Bunting, P., Hardy, A., Bell, G., 2019. Using continuous change detection and classification of landsat data to investigate long-term mangrove dynamics in the sundarbans region. Remote Sensing 11, 2833. https://doi.org/10.3390/rs11232833.
Belgiu, M., Drăguţ, L., 2016. Random forest in remote sensing: A review of applications and future directions. ISPRS Journal of Photogrammetry and Remote Sensing 114, 24–31. https://doi.org/10.1016/j.isprsjprs.2016.01.011.
Bonis, A., Bouzillé, J. aB, 2012. The project VegFrance: Towards a national vegetation database for France. Plant Sociology 49, 97–99.
Brinson, M., 1993. A Hydrogeomorphic Classification for Wetlands (Wetlands Research Program Technical Report No. WRP-DE-4). US Army Corps of Engineers.
Buck, O., Haub, C., Woditsch, S., Lindemann, M., Kleinwillinghöfer, L., Hazeu, G., Kosztra, B., Kleeschulte, S., Arnold, S., Hölzl, M., 2015. Analysis of the LUCAS nomenclature and proposal for adaptation of the nomenclature in view of its use by the Copernicus land monitoring services.: EEA/EFTAS. Contract No 3436/B2015/RO-COPERNICUS/EEA. 56195. EEA-European Environment Agency.
Chen, S., Woodcock, C.E., Bullock, E.L., Arévalo, P., Torchinava, P., Peng, S., Olofsson, P., 2021. Monitoring temperate forest degradation on google earth engine using landsat time series analysis. Remote Sensing of Environment 265, 112648. https://doi.org/10.1016/j.rse.2021.112648.
Chytrý, M., Tichý, L., Hennekens, S.M., Knollová, I., Janssen, J.A., Rodwell, J.S., Peterka, T., Marcenò, C., Landucci, F., Danihelka, J., 2020. EUNIS Habitat Classification: expert system, characteristic species combinations and distribution maps of European habitats. Applied Vegetation Science.
Clair, M., Gaudillat, V., Michez, N., Poncet, L., Poncet, L., 2017. HABREF v3. 1, référentiel des typologies d'habitats et de végétation pour la France. Guide méthodologique. Service du patrimoine naturel, Muséum national d'histoire naturelle, Paris.
Costa, H., 2022. mapaccuracy: Unbiased Thematic Map Accuracy and Area.
Crist, E.P., 1985. A TM tasseled cap equivalent transformation for reflectance factor data. Remote Sensing of Environment 17, 301–306.
Davidson, N.C., Dinesen, L., Fennessy, S., Finlayson, C.M., Grillas, P., Grobicki, A., McInnes, R.J., Stroud, D.A., 2019. A review of the adequacy of reporting to the

Ramsar Convention on change in the ecological character of wetlands. Marine and Freshwater Research 71, 117–126.
Davies, C.E., Moss, D., Hill, M.O., 2004. EUNIS Habitat Classification. European Environment Agency, Copenhagen.
Delassus, L., Magnanon, S., Colasse, V., Glemarec, E., Guitton, H., Laurent, E., Thomassin, G., Bioret, F., Catteau, E., Clément, B., Diquelou, S., Felzines, J., De Foucault, B., Gauberville, C., Gaudillat, V., Guillevic, Y., Haury, J., Royer, J., Vallet, J., Geslin, J., Goret, M., Hardegen, M., Lacroix, P., Reimringer, K., Sellin, V., Waymel, J., Zambettakis, C., 2014. Classification physionomique et phytosociologique des végétations de Basse-Normandie, Bretagne et Pays de la Loire. Conservatoire botanique national de Brest, Brest.
Delbosc, P., Lagrange, I., Rozo, C., Bensettiti, F., Bouzillé, J.-B., Evans, D., Lalanne, A., Rapinel, S., Bioret, F., 2021. Assessing the conservation status of coastal habitats under Article 17 of the EU Habitats Directive. Biological Conservation 254, 108935.
Demarquet, Q., Rapinel, S., Dufour, S., Hubert-Moy, L., 2023. Long-term wetland monitoring using the landsat archive: A review. Remote Sensing 15, 820. https://doi.org/10.3390/rs15030820.
Devillers, P., Devillers-Terschuren, J., Ledant, J., 1991. CORINE biotopes manual. Habitats of the European Community. Office for Official Publications of the European Communities, Luxembourg.
Duncan, P., Hewison, A.J.M., Houte, S., Rosoux, R., Tournebize, T., Dubs, F., Burel, F., Bretagnolle, V., 1999. Long-term changes in agricultural practices and wildfowling in an internationally important wetland, and their effects on the guild of wintering ducks. Journal of Applied Ecology 36, 11–23.
Dwyer, J.L., Roy, D.P., Sauer, B., Jenkerson, C.B., Zhang, H.K., Lymburner, L., 2018. Analysis Ready Data: Enabling Analysis of the Landsat Archive. Remote Sensing 10, 1363. https://doi.org/10.3390/rs10091363.
EEA, 2014. Crosswalk between EUNIS habitats classification and Corine land cover [WWW Document]. URL https://www.eea.europa.eu/data-and-maps/data/eunis-habitat-classification-1/documentation/eunis-clc.pdf.
European Court of Auditors, 2016. The Land Parcel Identification System: a useful tool to determine the eligibility of agricultural land – but its management could be further improved. Special report No 25, 2016. Publications Office of the European Union, LU.
Farr, T.G., Rosen, P.A., Caro, E., Crippen, R., Duren, R., Hensley, S., Kobrick, M., Paller, M., Rodriguez, E., Roth, L., Seal, D., Shaffer, S., Shimada, J., Umland, J., Werner, M., Oskin, M., Burbank, D., Alsdorf, D., 2007. The Shuttle radar topography mission. Reviews of Geophysics 45. https://doi.org/10.1029/2005RG000183.
Foga, S., Scaramuzza, P.L., Guo, S., Zhu, Z., Dilley Jr, R.D., Beckmann, T., Schmidt, G.L., Dwyer, J.L., Hughes, M.J., Laue, B., 2017. Cloud detection algorithm comparison and validation for operational Landsat data products. Remote Sensing of Environment 194, 379–390.
Friedl, M.A., Woodcock, C.E., Olofsson, P., Zhu, Z., Loveland, T., Stanimirova, R., Arevalo, P., Bullock, E., Hu, K.-T., Zhang, Y., Turlej, K., Tarrio, K., McAvoy, K., Gorelick, N., Wang, J.A., Barber, C.P., Souza, C., 2022. Medium spatial resolution mapping of global land cover and land cover change across multiple decades from landsat. Front. Remote Sens. 3 https://doi.org/10.3389/frsen.2022.894571.
Fritz, S., See, L., Perger, C., McCallum, I., Schill, C., Schepaschenko, D., Duerauer, M., Karner, M., Dresel, C., Laso-Bayas, J.-C., Lesiv, M., Moorthy, I., Salk, C.F., Danylo, O., Sturn, T., Albrecht, F., You, L., Kraxner, F., Obersteiner, M., 2017. A global dataset of crowdsourced land cover and land use reference data. Scientific Data 4, 170075. https://doi.org/10.1038/sdata.2017.75.
Fu, B., Lan, F., Yao, H., Qin, J., He, H., Liu, L., Huang, L., Fan, D., Gao, E., 2022. Spatio-temporal monitoring of marsh vegetation phenology and its response to hydro-meteorological factors using CCDC algorithm with optical and SAR images: In case of Honghe National Nature Reserve, China. Science of the Total Environment 843, 156990. https://doi.org/10.1016/j.scitotenv.2022.156990.
Fuller, R.M., Smith, G.M., Devereux, B.J., 2003. The characterisation and measurement of land cover change through remote sensing: problems in operational applications? International Journal of Applied Earth Observation and Geoinformation 4, 243–253. https://doi.org/10.1016/S0303-2434(03)00004-7.
Godet, L., Thomas, A., 2013. Three centuries of land cover changes in the largest French Atlantic wetland provide new insights for wetland conservation. Applied Geography 42, 133–139. https://doi.org/10.1016/j.apgeog.2013.05.011.
Gómez, C., White, J.C., Wulder, M.A., 2016. Optical remotely sensed time series data for land cover classification: A review. ISPRS Journal of Photogrammetry and Remote Sensing 116, 55–72. https://doi.org/10.1016/j.isprsjprs.2016.03.008.
Gorelick, N., Hancher, M., Dixon, M., Ilyushchenko, S., Thau, D., Moore, R., 2017. Google earth engine: Planetary-scale geospatial analysis for everyone. Remote Sensing of Environment, Big Remotely Sensed Data: Tools, Applications and Experiences 202, 18–27. https://doi.org/10.1016/j.rse.2017.06.031.
He, T., Fu, Y., Ding, H., Zheng, W., Huang, X., Li, R., Wu, S., 2022. Evaluation of mangrove wetlands protection patterns in the Guangdong-Hong Kong–Macao greater bay area using time-series landsat imageries. Remote Sensing 14, 6026. https://doi.org/10.3390/rs14236026.
Hotaiba, A.M., Salem, B.B., Halmy, M.W.A., 2024. Assessment of wetland ecosystem's health using remote sensing-case study: Burullus Wetland-Ramsar site. Estuaries and Coasts 47, 201–215.
Huang, Y., Peng, J., Sun, W., Chen, N., Du, Q., Ning, Y., Su, H., 2022. Two-branch attention adversarial domain adaptation network for hyperspectral image classification. IEEE Transactions on Geoscience and Remote Sensing 60, 1–13.
Huete, A., Didan, K., Miura, T., Rodriguez, E.P., Gao, X., Ferreira, L.G., 2002. Overview of the radiometric and biophysical performance of the MODIS vegetation indices. Remote Sensing of Environment, The Moderate Resolution Imaging Spectroradiometer (MODIS): a new generation of Land Surface Monitoring 83, 195–213. https://doi.org/10.1016/S0034-4257(02)00096-2.
IGN, Shom, 2009. Trait de côte Histolitt – v2.0, Descriptif technique. Institut Géographique National.
Jafarzadeh, H., Mahdianpari, M., Gill, E.W., Brisco, B., Mohammadimanesh, F., 2022. Remote sensing and machine learning tools to support wetland monitoring: a meta-analysis of three decades of research. Remote Sensing 14, 6104.
Ji, Y., Sun, W., Wang, Y., Lv, Z., Yang, G., Zhan, Y., Li, C., 2024. Domain adaptive and interactive differential attention network for remote sensing image change detection. IEEE Transactions on Geoscience and Remote Sensing.
Jiang, Z., Huete, A.R., Didan, K., Miura, T., 2008. Development of a two-band enhanced vegetation index without a blue band. Remote Sensing of Environment 112, 3833–3845. https://doi.org/10.1016/j.rse.2008.06.006.
Kennedy, R.E., Yang, Z., Cohen, W.B., 2010. Detecting trends in forest disturbance and recovery using yearly Landsat time series: 1. LandTrendr — Temporal segmentation algorithms. Remote Sensing of Environment 114, 2897–2910. https://doi.org/10.1016/j.rse.2010.07.008.
Key, C., Benson, N., 2006. Landscape Assessment: Ground measure of severity, the Composite Burn Index; and Remote sensing of severity, the Normalized Burn Ratio., in: FIREMON: Fire Effects Monitoring and Inventory System, General Technical Report. Ogden, UT, p. LA 1-51.
Liu, M., Liu, S., Ning, Y., Zhu, Y., Valbuena, R., Guo, R., Li, Y., Tang, W., Mo, D., Rosa, I. M., 2020. Co-evolution of emerging multi-cities: rates, patterns and driving policies revealed by continuous change detection and classification of landsat data. Remote Sensing 12, 2905.
Liu, K., Sun, W., Shao, Y., Liu, W., Yang, G., Meng, X., Peng, J., Mao, D., Ren, K., 2022. Mapping coastal wetlands using transformer in transformer deep network on China ZY1-02D hyperspectral satellite images. IEEE Journal of Selected Topics in Applied Earth Observations and Remote Sensing 15, 3891–3903.
Liu, Q., Zhang, Y., Liu, L., Wang, Z., Nie, Y., Rai, M.K., 2021. A novel Landsat-based automated mapping of marsh wetland in the headwaters of the Brahmaputra, Ganges and Indus Rivers, southwestern Tibetan Plateau. International Journal of Applied Earth Observation and Geoinformation 103, 102481.
Myneni, R.B., Hall, F.G., Sellers, P.J., Marshak, A.L., 1995. The interpretation of spectral vegetation indexes. IEEE Transactions on Geoscience and Remote Sensing 33, 481–486. https://doi.org/10.1109/TGRS.1995.8746029.
Olofsson, P., Foody, G.M., Herold, M., Stehman, S.V., Woodcock, C.E., Wulder, M.A., 2014. Good practices for estimating area and assessing accuracy of land change. Remote Sensing of Environment 148, 42–57. https://doi.org/10.1016/j.rse.2014.02.015.
Palmieri, A., 2016. Integrating statistical and geographical information: LUCAS survey, a case study for land monitoring in European Union, in: UNECE Conference of European Statisticians Workshop on Statistical Data Collection.
Pasquarella, V.J., Arévalo, P., Bratley, K.H., Bullock, E.L., Gorelick, N., Yang, Z., Kennedy, R.E., 2022. Demystifying LandTrendr and CCDC temporal segmentation. International Journal of Applied Earth Observation and Geoinformation 110, 102806. https://doi.org/10.1016/j.jag.2022.102806.
Peng, J., Liu, S., Lu, W., Liu, M., Feng, S., Cong, P., 2021. Continuous change mapping to understand wetland quantity and quality evolution and driving forces: A case study in the liao river estuary from 1986 to 2018. Remote Sensing 13, 4900. https://doi.org/10.3390/rs13234900.
Petit, T., Sigwalt, A., Martel, G., Couvreur, S., 2022. The place of grasslands in cattle farmers' perceptions of forage production: Useful insights of 10 years of empirical research on grasslands. Sustainability 14, 12309. https://doi.org/10.3390/su141912309.
Potapov, P.V., Turubanova, S.A., Hansen, M.C., Adusei, B., Broich, M., Altstatt, A., Mane, L., Justice, C.O., 2012. Quantifying forest cover loss in Democratic Republic of the Congo, 2000–2010, with Landsat ETM+ data. Remote Sensing of Environment 122, 106–116.
Pouzet, P., Creach, A., Godet, L., 2015. Dynamique de la démographie et du bâti dans l'ouest du Marais poitevin depuis 1705. Norois. Environnement, aménagement, société 83–96. https://doi.org/10.4000/norois.5589.
QGIS Development Team, 2018. QGIS Version 2.18. 22. Geographic Information System.
Rapinel, S., Bouzillé, J.-B., Oszwald, J., Bonis, A., 2015. Use of bi-seasonal landsat-8 imagery for mapping marshland plant community combinations at the regional scale. Wetlands 35, 1043–1054. https://doi.org/10.1007/s13157-015-0693-8.
Rapinel, S., Clément, B., Dufour, S., Hubert-Moy, L., 2018. Fine-scale monitoring of long-term wetland loss using LiDAR data and historical aerial photographs: The example of the couesnon floodplain, france. Wetlands 38, 423–435.
Regnauld, H., Costa, S., Musereau, J., 2015. Spits on the French atlantic and channel coasts: morphological behaviour and present management policies. Sand and Gravel Spits 247–258.
Robert, S., Brosseau, O., 2022. Principaux types de données mis à disposition du public sur le site de l'Inventaire national du patrimoine naturel (INPN) : V2. (No. mnhn-04148916). PatriNat (OFB-CNRS-MNHN).
Skidmore, A.K., Coops, N.C., Neinavaz, E., Ali, A., Schaepman, M.E., Paganini, M., Kissling, W.D., Vihervaara, P., Darvishzadeh, R., Feilhauer, H., Fernandez, M., Fernández, N., Gorelick, N., Geijzendorffer, I., Heiden, U., Heurich, M., Hobern, D., Holzwarth, S., Muller-Karger, F.E., Van De Kerchove, R., Lausch, A., Leitão, P.J., Lock, M.C., Mücher, C.A., O'Connor, B., Rocchini, D., Roeoesli, C., Turner, W., Vis, J. K., Wang, T., Wegmann, M., Wingate, V., 2021. Priority list of biodiversity metrics to observe from space. Nature Ecology & Evolution 5, 896–906. https://doi.org/10.1038/s41559-021-01451-x.
Souza Jr, C.M., Roberts, D.A., Cochrane, M.A., 2005. Combining spectral and spatial information to map canopy damage from selective logging and forest fires. Remote Sensing of Environment 98, 329–343.
Sun, W., Liu, K., Ren, G., Liu, W., Yang, G., Meng, X., Peng, J., 2021. A simple and effective spectral-spatial method for mapping large-scale coastal wetlands using

China ZY1-02D satellite hyperspectral images. International Journal of Applied Earth Observation and Geoinformation 104, 102572.
Tibshirani, R., 1996. Regression shrinkage and selection via the lasso. Journal of the Royal Statistical Society: Series B (methodological) 58, 267–288. https://doi.org/10.1111/j.2517-6161.1996.tb02080.x.
USGS, 2021. Landsat collection 2 (Report No. 2021–3002), Fact Sheet. Reston, VA. https://doi.org/10.3133/fs20213002.
Wang, H., Zhou, Y., Wu, J., Wang, C., Zhang, R., Xiong, X., Xu, C., 2023. Human activities dominate a staged degradation pattern of coastal tidal wetlands in Jiangsu province. China. Ecological Indicators 154, 110579. https://doi.org/10.1016/j.ecolind.2023.110579.
Wulder, M.A., Roy, D.P., Radeloff, V.C., Loveland, T.R., Anderson, M.C., Johnson, D.M., Healey, S., Zhu, Z., Scambos, T.A., Pahlevan, N., 2022. Fifty years of Landsat science and impacts. Remote Sensing of Environment 280, 113195.
Xie, S., Liu, L., Zhang, X., Yang, J., 2022. Mapping the annual dynamics of land cover in Beijing from 2001 to 2020 using Landsat dense time series stack. ISPRS Journal of Photogrammetry and Remote Sensing 185, 201–218. https://doi.org/10.1016/j.isprsjprs.2022.01.014.
Xu, X., Chen, M., Yang, G., Jiang, B., Zhang, J., 2020. Wetland ecosystem services research: A critical review. Global Ecology and Conservation 22, e01027.
Yang, R., Chen, Y., Qiu, Y., Lu, K., Wang, X., Sun, G., Liang, Q., Song, H., Liu, S., 2023. Assessing the landscape ecological health (LEH) of wetlands: Research content and evaluation methods (2000–2022). Water 15, 2410.
Yang, X., Zhu, Z., Qiu, S., Kroeger, K.D., Zhu, Z., Covington, S., 2022. Detection and characterization of coastal tidal wetland change in the northeastern US using Landsat time series. Remote Sensing of Environment 276, 113047. https://doi.org/10.1016/j.rse.2022.113047.
Ye, S., Zhu, Z., Cao, G., 2023. Object-based continuous monitoring of land disturbances from dense Landsat time series. Remote Sensing of Environment 287, 113462. https://doi.org/10.1016/j.rse.2023.113462.
Zhang, Y., Woodcock, C.E., Arévalo, P., Olofsson, P., Tang, X., Stanimirova, R., Bullock, E., Tarrio, K.R., Zhu, Z., Friedl, M.A., 2022. A global analysis of the spatial and temporal variability of usable landsat observations at the pixel scale. Front. Remote Sens. 3 https://doi.org/10.3389/frsen.2022.894618.
Zhu, Z., 2017. Change detection using landsat time series: A review of frequencies, preprocessing, algorithms, and applications. ISPRS Journal of Photogrammetry and Remote Sensing 130, 370–384. https://doi.org/10.1016/j.isprsjprs.2017.06.013.
Zhu, Z., Woodcock, C.E., 2014a. Continuous change detection and classification of land cover using all available Landsat data. Remote Sensing of Environment 144, 152–171.
Zhu, Z., Woodcock, C.E., 2014b. Automated cloud, cloud shadow, and snow detection in multitemporal Landsat data: An algorithm designed specifically for monitoring land cover change. Remote Sensing of Environment 152, 217–234. https://doi.org/10.1016/j.rse.2014.06.012.
Zhu, Z., Woodcock, C.E., Holden, C., Yang, Z., 2015. Generating synthetic Landsat images based on all available Landsat data: Predicting Landsat surface reflectance at any given time. Remote Sensing of Environment 162, 67–83. https://doi.org/10.1016/j.rse.2015.02.009.